Transition-metal granular solids: Microstructure, magnetic properties, and giant magnetoresistance

Jian-Qing Wang and Gang Xiao
Department of Physics, Brown University, Providence, Rhode Island 02912
(Received 14 September 1993)

We have systematically investigated the magnetotransport properties of five binary metallic systems (Co-Ag, Fe-Ag, Fe-Cu, Fe-Au, and Fe-Pt). Except for Fe-Pt, which forms a solid solution in sputtering synthesis, all other systems exhibit giant magnetoresistance (GMR) effects and are immiscible or almost immiscible alloys. Using a combination of structural analysis involving transmission electron microscopy, x-ray diffraction, and magnetic characterization, we have revealed the microstructure for some of the granular alloys where the magnetic particles are embedded in a nonmagnetic matrix. Across the whole particle volume-fraction range ($0 \leq x \leq 100\,\%$), a universal peak of GMR at $x = 0.15$–0.25 is uncovered in every granular system. The suppression of GMR in the high-x region is attributed to the percolation effect, which also causes a concurrent reduction in magnetic coercivity. Magnetic particle size, a variable under thermal annealing, is another important factor affecting GMR. We have observed correlations between transport properties and particle size, supporting the view that magnetic scattering occurs predominantly on the surface of the particles. Quantitatively, both the field and temperature dependence of the GMR effect can be well accounted for by a modified exchange-interaction model. Spin-wave excitation and electron-phonon interaction at finite temperatures are detrimental to GMR. Superparamagnetism and large magnetic anisotropy impede the saturation process of GMR, but have no effect on the saturated value of GMR.

I. INTRODUCTION

The giant magnetoresistance (GMR) effect was first discovered in magnetic multilayers (e.g., Fe-Cr, Co-Cu)[1–6] and subsequently in magnetic heterogeneous alloys with ferromagnetic granules embedded in nonmagnetic metals.[7–9] It was found that the resistance of these materials exhibits large changes upon the application of an external magnetic field. The changes can be of the same order of magnitude as the resistance itself, rendering the effect extraordinary when compared with the much smaller magnetoresistance (MR) in nonmagnetic metals. In the latter case the MR is due to the direct effect of the magnetic field on the conduction electrons through modification of the electron-orbit or spin-orbit interaction[10–12] and on the potential of the scattering centers. In the case of GMR, it is believed to be a manifestation of spin-dependent scattering. The main effect of the applied magnetic field is to reorient the ferromagnetic components to a macroscopically aligned state, and thus generate a magnetic disorder-order transition. GMR is the extra resistance due to the scattering of electrons off nonaligned ferromagnetic components.

The interest in studying GMR in magnetic inhomogeneous systems, e.g., multilayers and granular materials, stems not only from its potential application in magnetic sensors, but also from the need to understand the fundamental underlying mechanism of the anomalous magnetotransport properties in these systems. Theoretical investigations of the effect have been carried out for multilayers using both the quasiclassical Boltzmann approach[13] and the quantum Kubo formalism,[14,15] and for granular systems using the quantum model.[16] A study has shown that the quasiclassical Boltzmann approach and the quantum Kubo treatment are in fact equivalent for the case of multilayers, provided the scattering at the interface is treated properly.[17] One expects that the same applies to a system of granular materials.

On the experimental front there exist extensive studies on the GMR effect in multilayer systems, but similar investigations in granular materials are still in their infancy. Although granular solids rival the best multilayers in terms of the magnitude of the GMR effect, we do not have a good understanding of the magnetotransport in these highly random and heterogeneous systems. The complexity involved is very challenging to experimental and theoretical efforts alike. Nevertheless, granular solids should provide a stringent test to various models dealing with complex systems. These materials also enjoy many advantages over multilayers and other systems. They are very easy to fabricate and their microstructure can be easily altered by postfabrication thermal treatment.

Although the GMR effect has been reported in many granular systems, what is still lacking is a detailed and systematic investigation of this effect in granular systems, covering microstructural, magnetic, and magnetotransport properties. We have undertaken such a task with the objective of experimentally exploring many granular systems with a wide range of particle volume fraction and thermal treatment conditions. We have utilized a large array of experimental techniques including transmission electron microscopy (TEM), x-ray diffraction, superconducting quantum interference device (SQUID) magnetometry, magnetoresistivity, and Hall-effect mea-

 ©1994 The American Physical Society

surements. A comprehensive set of data was obtained, allowing us to uncover various universal behaviors and correlations in the GMR effect with other variables of structure and interactions. We are also able to test an extended model of magnetic dilute alloys and find that it accounts for the GMR effect very well in granular systems.

Our systems of interests are Co-Ag, Fe-Ag, Fe-Cu, Fe-Au, and Fe-Pt. Except for Fe-Pt, the systems are immiscible or almost immiscible alloys under equilibrium.[18] This makes it possible to fabricate phase-separated heterogeneous alloys with ferromagnetic granules embedded in a nonmagnetic matrix. Phase separation is found to be essential to the GMR effect. Fe-Pt, which is a solid solution, does not exhibit GMR.

This paper is organized as follows: In the next section sample fabrication and preparation are described. In Sec. III, we present the characterization of microstructures via TEM and x-ray diffraction measurements. The measured magnetic properties and the derived magnetic structural information for the magnetic granules are presented in Sec. IV, where results from each technique are compared to obtain a coherent picture of the microstructure. In Sec. V, we give a comprehensive presentation of the experimental results of our magnetotransport studies on several granular systems with various volume fractions and annealing conditions. Results of magnetoresistivity ρ_{xx}, Hall resistivity ρ_{xy}, and the magnetization M at different measuring temperatures are discussed. In Sec. VI, we introduce a modified effective exchange-interaction model and use it to analyze the magnetotransport properties. We conclude this paper in Sec. VII.

II. SAMPLE FABRICATION AND PREPARATION

The samples used in our study were fabricated on Si substrates using the magnetron-sputtering technique. Our high-vacuum system is equipped with a cluster of three magnetron guns aimed at the same spot and several independent sputtering guns. To obtain samples with varying volume fractions we used the magnetron co-sputtering method. Two of the collimated cluster guns were loaded with pure magnetic and nonmagnetic targets respectively ($\geq 99.9\%$) and were co-sputtered. The variable content of each sample was achieved by varying the relative sputtering rates of the two targets. Using rotatable multiple substrate holders we were able to obtain several samples with different volume fractions in a single run. In addition to co-sputtering, some samples were fabricated by using a single magnetron gun loaded with a composite target with a fixed composition. Before each run, the background vacuum was better than 1×10^{-7} Torr. The Ar sputtering gas pressure was kept at 4.0 mTorr by a gas-flow controller. All samples of the Fe-based series were deposited at ambient substrate temperature, while the Co-Ag samples were deposited at liquid-nitrogen temperature. The sputtering rate was about 2–3 Å/s. The typical film thickness was in the range of 0.2–1.0 μm. Postdeposition thermal annealing was carried out under high vacuum with a pressure less than 1×10^{-7} Torr. The annealing duration was 15 minutes at a chosen annealing temperature T_A with a ramp rate of 10 °C/min and natural cooling. For direct TEM observation, thin-film ($\leq$ 500 Å) specimens were deposited directly onto carbon-coated copper grids. The standard photolithography and wet-etching techniques were used to pattern samples into a Hall-bar configuration for electrical measurement. Samples for magnetic and x-ray measurements were taken near the same location as those for electrical measurements to achieve best correspondence among these measurements.

III. MICROSTRUCTURE

In order to study their anomalous magnetotransport properties it is necessary to gain a good understanding of the microstructure of the granular systems. For this reason, we have investigated the structural characteristics of a series of annealed samples by using TEM, x-ray diffraction and magnetic measurements. TEM provides us with information of grain size, shape, and distribution. To find out the phase and structure of an individual grain, one has to rely on a TEM microdiffraction technique that involves focusing an electron beam onto a particular grain of interest. In general, TEM best combines real-space imaging with reciprocal-space diffraction techniques to obtain information on the microstructure of multicomponent granular materials.

X-ray diffraction is also very useful in phase identification and structural determination. The spectral linewidths can provide estimates of the average grain size of a particular phase. Magnetic measurement of granular systems proves to be highly informative for microstructure characterization.[19] At high temperatures, magnetic granules are in the superparamagnetic state. The saturation process of the magnetization and the temperature dependence of the initial susceptibility are determined by the size of the magnetic granules. Analysis of these magnetic data, therefore, gives information about the magnetic particle size. We will provide the results and analysis of the magnetic measurement in Sec. IV.

A. Transmission electron microscopy

The TEM and electron microdiffraction were performed with a Philips EM420T microscope. For the structural characterization we have concentrated on a series of $Fe_{20}Ag_{80}$ samples with various thermal treatments. This particular composition yields the maximum GMR effect in the Fe-Ag series. Figures 1(a)–(d) are some representative plane-view TEM micrographs showing the microstructure of $Fe_{20}Ag_{80}$ with T_A as sputtered, and 200, 400, and 500 °C. Also shown in the upper right corners are the corresponding selected-area diffraction patterns. Even in the as-sputtered sample, grain structure can be clearly seen with an average size of about 30 Å. The diffraction pattern reflects the crystalline nature of the film. All the spectral rings can be indexed as those of Ag fcc crystallites. The widths of the lines are broad due to the small grain size.

As the temperature increases, the grain size becomes progressively larger. At $T_A = 500\,^{\circ}\mathrm{C}$, the average grain size is on the order of 350 Å. Figure 2 presents some relevant size or length parameters for the $Fe_{20}Ag_{80}$ samples annealed at different T_A's. The average grain sizes determined from TEM are shown as open circles. It is seen that thermal annealing is an effective way to enlarge the grain. The diffraction rings become sharper and more spotty at high T_A's, another indication of the existence of large grains.

With its high vapor-quenching rate, the sputtering technique can produce metastable crystalline or amorphous alloys with otherwise immiscible elements un-

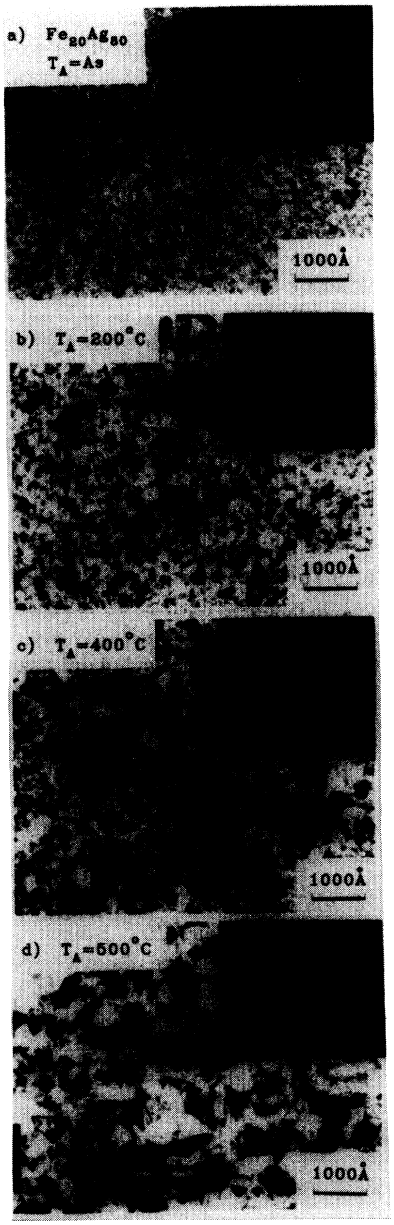

FIG. 1. Bright-field (TEM) images and selected-area diffraction patterns for $Fe_{20}Ag_{80}$ samples annealed at various temperatures T_A. (a) as-sputtered sample, (b) 200 °C, (c) 400 °C, and (d) 500 °C.

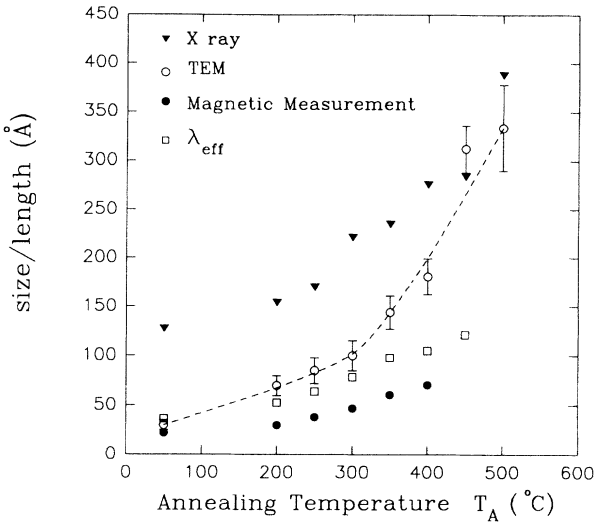

FIG. 2. Various determined size and length scales of $Fe_{20}Ag_{80}$ samples versus annealing temperature T_A. Results are given for grain sizes measured with x-ray diffraction (filled triangles) and TEM (open circles), magnetic particle sizes by magnetic measurements (filled circles), and effective mean free path λ_{eff} at $T = 4.2$ K by transport measurements (open squares).

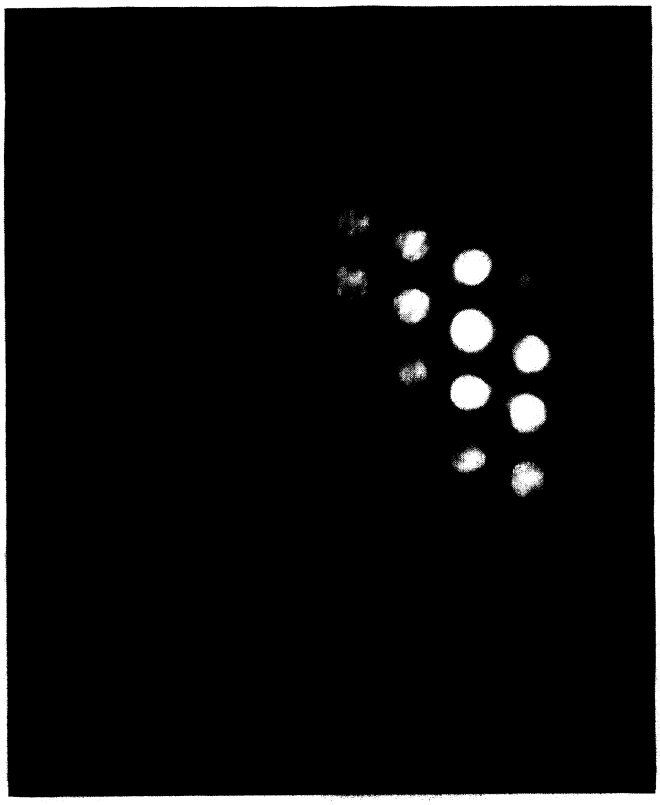

FIG. 3. Microdiffraction pattern of a Ag grain with zone axis [111] parallel to the electron beam.

der equilibrium conditions.[20–23] Appropriate thermal annealing induces phase separation and generates granular solids. In the Fe-Ag system we have evidence from magnetic measurements that phase separation in fact occurs in as-sputtered samples, as will be shown later. Unfortunately, it is difficult to determine the Fe and Ag phase separation by electron or x-ray diffraction, because the spectral lines of Fe overlap with some of the Ag lines within the resolution of our instrument, in particular because of the line broadening of our samples due to small grain sizes. We have also used the technique of electron microdiffraction, trying to identify the structure of individual grains. An electron beam of ~ 100 Å in diameter is focused on a particular grain of interest. The diffraction pattern thus obtained is from that grain and reflects its crystalline structure and orientation. Figure 3 shows the microdiffraction pattern from a selected grain. The diffraction pattern represents an fcc Ag grain with [011] zone axis parallel to the electron beam. We have made an extensive effort to determine phase and structural information on numerous grains at different locations on the 500 °C TEM sample. Almost all of the grains studied are definitive fcc Ag crystallites, matching precisely the symmetry and the lattice constant of the bulk Ag. Only in one case does the grain resemble the phase of bcc α-Fe. To reconcile this with the unequivocal evidence of the existence of Fe particles from magnetic measurements, we are led to conclude that the Fe particles have a much smaller size than the Ag grain size and that the Fe particles are mostly embedded in the Ag matrix.

B. X-ray diffraction

Every sample studied was checked by x-ray diffraction. In the case of $Fe_{20}Ag_{80}$, we observe that the spectra show the fcc structure throughout the whole range of annealing temperatures, consistent with the electron-diffraction result. Comparing with the relative spectral intensities of random polycrystalline Ag powder,[24] we find that the samples are [111] textured, i.e., the grains are predominantly [111] oriented. This is consistent with the TEM observation that it is most common to observe a [111]-oriented Ag grain in the microdiffraction mode. The estimated grain sizes from the [111] spectral linewidth are presented in Fig. 2 as filled triangles. Phase separation induced by thermal annealing has been convincingly identified in Fe-Cu and Co-Ag granular systems by using x-ray diffraction.[8,25] In the Fe-Ag system, on the other hand, phase separation is very difficult to identify for two reasons. First, the atomic number Z of Fe is much smaller than that of Ag, making the signal from the Fe phase harder to detect, particularly in the low-Fe-concentration region. Secondly, α-Fe spectral lines overlap with some of the Ag lines in our 2θ window, making α-Fe identification impossible with our spectrometer.

IV. MAGNETIC PROPERTIES

The study of the magnetic properties of granular materials with GMR is very important for two reasons. First, the magnetotransport properties depend directly on the magnetic state of the magnetic particles. Second, the magnetic properties are largely due to the magnetic component and are, therefore, sensitive to the size and shape of the magnetic particles. Studying the magnetic properties of granular materials opens another avenue to inspect their microstructure. Using a SQUID magnetometer, we have measured the field dependence of magnetization at various temperatures and the temperature dependence of the initial susceptibility in many samples.

We have relied on the measurement of magnetization and susceptibility to obtain the particle sizes of the magnetic component in $Fe_{20}Ag_{80}$ samples, as well as other magnetic quantities, e.g., saturation magnetization and coercivity. The magnetization curves are shown in Fig. 4 for $Fe_{20}Ag_{80}$ samples with T_A as sputtered (As), and 200 and 300 °C. The magnetizations measured with field both perpendicular (triangles) and parallel (circles) to the sample plane are presented for measurement temperatures at 5 K (upper graphs), 77 K (middle), and 300 K (lower). At $T = 5$ K, the saturation magnetization M_s of these samples was about 200 emu/g_{Fe}, a value consistent with M_s=221.2 emu/g_{Fe} of bulk Fe at $T = 0$ K.[26] This indicates that the Fe particles are rather pure in phase inside the Ag matrix. Otherwise, if there were alloy formation between Fe and Ag or if Fe were in non-α phase, M_s of the particles would be substantially different from the bulk value.

It is well known that below a critical size of a few hundred angstroms (depending on shape and internal anisotropy), an Fe particle forms a magnetic single-

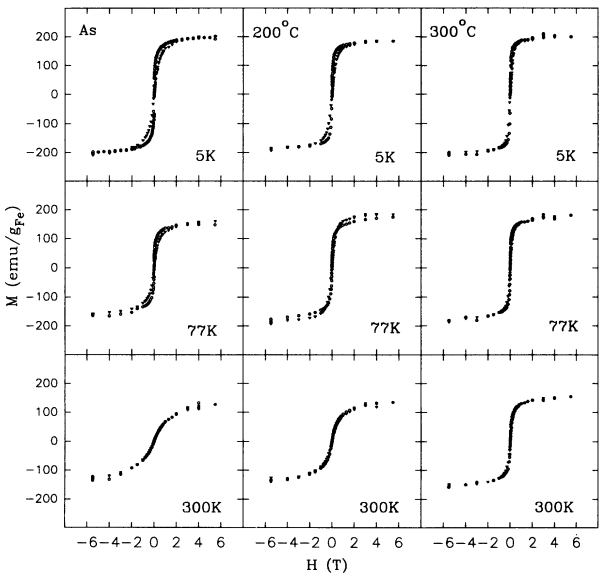

FIG. 4. Measured magnetization M (in units of emu/g_{Fe}) versus field $H(T)$. Results are presented for $Fe_{20}Ag_{80}$ samples as sputtered (first column), with $T_A = 200$ °C (second column), and $T_A = 300$ °C (third column). The measuring temperatures are 5 K (upper panels), 77 K (middle panels), and 300 K (lower panels). In each graph, data include perpendicular (triangles) and parallel (circles) field orientations with respect to the sample plane.

domain structure with the atomic spins aligned uniformly across the volume of the particle. At low temperatures, the giant moment of the Fe particle is frozen along the magnetic easy axis determined by the combined shape, strain, and crystalline anisotropies. The temperature below which this happens is called the blocking temperature. At higher temperatures, as the thermal energy surpasses the magnetic anisotropy energy of the particles, the moments of the particles fluctuate freely as in a paramagnetic system with each particle bearing a giant moment. Under the assumption of weak interparticle interactions, the magnetization curve $M(H)$ of such a superparamagnetic system with uniform particle size is described by the Langevin equation:

$$M = M_s \coth\left(\frac{\mu H}{k_B T}\right) - M_s \frac{k_B T}{\mu H}, \tag{1}$$

where μ $(= M_s V)$ is the magnetic moment of a single particle with volume V. Fitting the measurement results with this function, we can obtain, simultaneously, the magnetic moment μ per particle and M_s for T above the blocking temperature. The fitted values of μ and M_s(300 K) at 300 K for $Fe_{20}Ag_{80}$ samples annealed at various temperatures are listed in Table I.

It can be seen that the M_s of Fe particles at $T = 300$ K is much smaller than the corresponding M_s=217.8 emu/g_{Fe} for bulk[27] Fe at $T = 300$ K. This is consistent with an earlier observation that spin waves in small particles are softened substantially due to the magnetic-surface effect and the finite-size effect.[19] For single-domain particles, $\mu = M_s V$. Therefore, from measured μ and M_s one can calculate the average magnetic particle size (or volume V). We list the average number of Fe atoms and the diameter of the Fe particles in Table I, assuming that the particles are spherical.

The superparamagnetism which validates the aforementioned treatment is affected by the blocking effect which has its origin in the magnetic anisotropy energy of the magnetic particles. The thermal agitation or magnetic force is resisted by the anisotropy field experienced by these particles. We observe in Fig. 4 that at low temperatures (5 and 77 K) the measured magnetization shows anisotropy with respect to the orientation of the applied magnetic field. The magnetization is harder to saturate with the magnetic field perpendicular to the sample plane.

As a self-consistency check, the initial susceptibility χ as a function of T can also be used to determine the magnetic particle size. One can derive from the Langevin equation (1) that the susceptibility measured in the low-field limit is given by Curie's law:

$$\chi = \frac{M}{H} = \frac{M_s(T)\mu}{3k_B T} = \frac{M_s^2(T)V}{3k_B T} \quad \text{for } k_B T > \mu H. \tag{2}$$

The above formula assumes no magnetic interactions among the particles. In reality, especially at low temperatures, there are some spin correlations between particles. Chantrel and Wohlfarth have theoretically investigated the interaction effect on the magnetic susceptibility of ultrafine particle systems.[28] They found that χ can be described by a Curie-Weiss-type law:

$$\chi = \frac{M_s^2(T)V}{3k_B(T - T_0)} \quad \text{for } k_B T > \mu H, \tag{3}$$

where the parameter T_0 reflects the strength of the interaction and is called the effective Curie temperature. T_0 is in fact the intercept of $1/\chi \to 0$ at the T axis. In a superparamagnetic system, $M_s(T)$ is temperature dependent because of spin-wave excitations inside the single-domain particles at finite temperatures. From relation (3), one can plot $\{\chi(T - T_0)\}^{1/2} = \sqrt{\frac{V}{3k_B}} M_s(T)$ as a function of T, and then extrapolate the curve to $T \to 0$ K. The intercept is $\sqrt{\frac{V}{3k_B}} M_s(0)$. Since M_s at low T has been obtained in the magnetization measurements, we can deduce the volume V of the particles from the intercept.

We have measured $\chi(T)$, at a field of 100 G, of the $Fe_{20}Ag_{80}$ system annealed at various temperatures. The T dependence of $\chi(T)$ is displayed in Fig. 5 for a representative $Fe_{20}Ag_{80}$ sample annealed at 200 °C. Below the blocking temperature $T_B \sim 45$ K, the strong irreversibility between the zero-field-cooled and the field-cooled process is evident. However, in the region $T > T_B$, the system exhibits a reversible superparamagnetic behavior and is found to follow relation (3) very well. In the inset, we plot $[\chi(T - T_0)]^{1/2}$, which is proportional to $M_s(T)$ and $V^{1/2}$, against T. The slight T dependence of $[\chi(T - T_0)]^{1/2}$ is due to $M_s(T)$. From the intercept of $[\chi(T - T_0)]^{1/2}$ at $T = 0$ K, we can calculate the particle volume V, from which the diameter of the Fe particles and the number of Fe atoms per particle are obtained and listed in Table I. The calculated particle sizes agree

TABLE I. Structural and magnetic parameters determined from magnetic measurement for the $Fe_{20}Ag_{80}$ samples annealed at various temperatures T_A. μ/μ_B: magnetic moment of the magnetic particles in units of Bohr magneton; M_s: saturation magnetization in units of emu/g_{Fe}; N: number of Fe atoms per particle; and $2r_o$: diameter of the particles in Å.

T_A	Magnetization (300 K)				Susceptibility		
	μ/μ_B	M_s	N	$2r_0$	M_s(5 K)	N	$2r_0$
As	596	143	400	21	210	642	24
200 °C	1492	139	1073	29	187	1327	31
250 °C	2828	137	2049	36	173	3257	42
300 °C	6066	141	5654	50	196	4364	46
350 °C	1.30×10^4	142	9147	59	186	1.02×10^4	62
400 °C	1.75×10^4	112	15511	71	146		

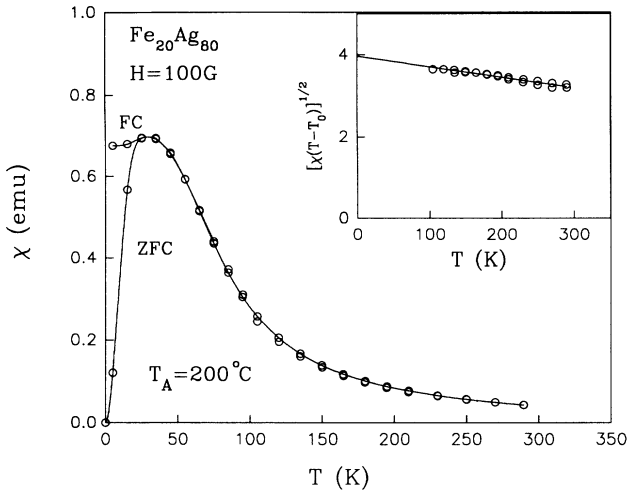

FIG. 5. Magnetic susceptibility χ as a function of temperature T for $Fe_{20}Ag_{80}$ ($T_A = 200\,^{\circ}C$) in both zero-field-cooled and field-cooled modes. In the inset, $[\chi(T - T_0)]^{\frac{1}{2}}$ is shown against T, where T_0 is the effective Curie temperature. The intercept at $T = 0$ K provides the information about particle size.

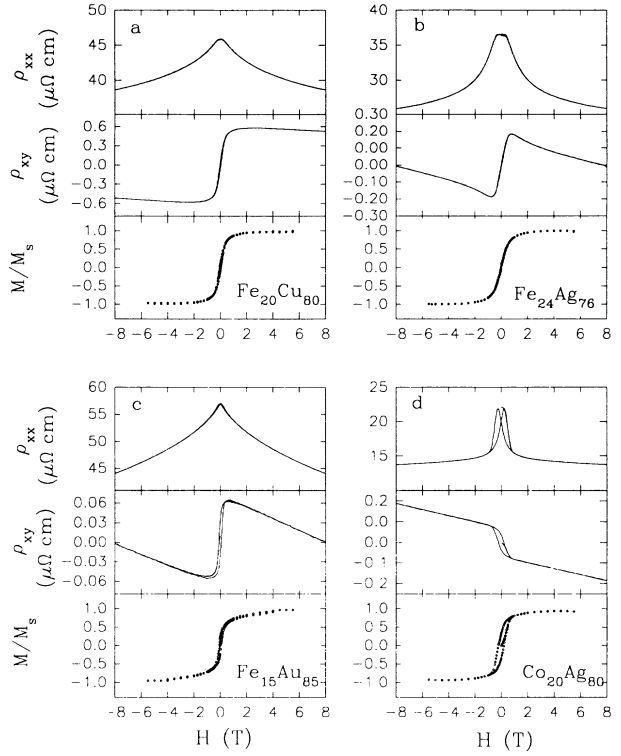

FIG. 6. Resistivity ρ_{xx} (upper panels), Hall resistivity ρ_{xy} (middle panels), and normalized magnetization M/M_s (lower panels) versus magnetic field at $T = 4.2$ K for (a) $Fe_{20}Cu_{80}$, (b) $Fe_{24}Ag_{76}$, (c) Fe_{15} Au_{85}, and (d) $Co_{20}Ag_{80}$.

well with those obtained from magnetization measurements. Also listed in Table I are low-temperature saturation magnetizations $M_s(5\text{ K})$.

We have presented the magnetic particle size obtained from magnetization and susceptibility measurements in Fig. 2 as filled circles. It is clear that the magnetic particle sizes in our $Fe_{20}Ag_{80}$ system are much smaller than the average grain sizes determined by TEM and x-ray diffraction. Magnetic measurement is, therefore, highly complimentary to other structural characterization techniques.

V. EXPERIMENTAL RESULTS OF MAGNETOTRANSPORT PROPERTIES

For each sample prepared, we have measured both the resistivity ρ_{xx} and the Hall resistivity ρ_{xy} as functions of the magnetic field at three temperatures, $T = 4.2$, 77, and 300 K. Because of magnetic hysteresis, the magnetotransport measurement was done in a sweeping magnetic field ($0 \rightarrow 8 \rightarrow -8 \rightarrow 0$ T). Table II lists electrical transport parameters for all of the samples with varying compositions or thermal history. To understand the parameters in Table II, we show some typical results of $\rho_{xx}(H)$, $\rho_{xy}(H)$, and the normalized magnetization $M(H)/M_s$ in Fig. 6 for the as-sputtered samples of $Fe_{20}Cu_{80}$, $Fe_{24}Ag_{76}$, $Fe_{15}Au_{85}$, and for $Cu_{20}Ag_{80}$ annealed at 200 °C. These samples tend to exhibit a maximum GMR in their corresponding series.

As shown in Fig. 6, relatively large values of MR are realized in transition-metal granular systems. In some systems such as $Co_{20}Ag_{80}$, MR can be saturated with a field of about 1 T, whereas in other systems, MR remains unsaturated even at our maximum field of 8 T. In the literature, a common parameter to characterize MR is $\Delta\rho_{xx}/\rho_{xx}$, where $\Delta\rho_{xx}$ is the difference in ρ_{xx} between the zero-field value and the saturated value, and ρ_{xx} is chosen as either the zero-field value or the saturated value. In this paper, we define $\Delta\rho_{xx}/\rho_{xx}$ as

$$\Delta\rho_{xx}/\rho_{xx} = [\rho_{xx}(0\text{ T}) - \rho_{xx}(8\text{ T})]/\rho_{xx}(0)\ . \qquad (4)$$

This definition gives a smaller $\Delta\rho_{xx}/\rho_{xx}$ value than other definitions since $\rho_{xx}(0)$ is a maximum at $H = 0$. The maximum GMR values in our as-sputtered series of Fe_xAg_{100-x}, Co_xAg_{100-x}, Fe_xCu_{100-x}, and Fe_xAu_{100-x} are 30%, 46%, 16%, and 23% respectively at $T = 4.2$ K. The values of $\Delta\rho_{xx}/\rho_{xx}$ for all of the samples are provided in Table II. Also listed in Table II are $\rho_{xx}(0)$ and $\Delta\rho_{xx}$. Although commonly used in the literature, $\Delta\rho_{xx}/\rho_{xx}$ is not the best parameter to characterize GMR because $\rho_{xx}(0)$ also contains contributions from disorder and other nonmagnetic scattering. $\Delta\rho_{xx}$, on the other hand, is mainly due to magnetic scattering.

The Hall resistivity ρ_{xy} shown in the middle panels of Fig. 6 consists of two parts for these samples, i.e., $\rho_{xy} = \rho^0_{xy} + \rho^s_{xy}$. The initial sharp rise in ρ_{xy} in the low-field region is primarily due to the extraordinary Hall effect (EHE) component ρ^s_{xy}, which is a distinctive feature of ferromagnetic systems.[29] This component arises from the left-right asymmetry in electron scattering and is proportional to the magnetization M, i.e.

$$\rho^s_{xy} = R_s 4\pi M, \qquad (5)$$

where R_s is the extraordinary Hall coefficient and is ma-

TABLE II. Electrical transport parameters obtained from measurements for Fe-Ag, Fe-Cu, Fe-Au, and Co-Ag systems. The content of each component is specified by its volume fraction. T_A: annealing temperature (As—as sputtered at ambient temperature, ~50 °C); T: measurement temperature; SM: sputtering mode (I—single target, II—co-deposition); MR (%): magnetoresistance defined in relation (4) in the text; $\rho_{xx}(0)$: resistivity at zero field; $\Delta\rho_{xx}$: net change in resistivity between $H = 0$ and 8 T; n_H: Hall number due to normal Hall effect; λ_{eff}: effective mean free path (n_H and λ_{eff} are determined from Hall-effect and resistivity measurements).

Sample	T_A (°C)	T (K)	SM	MR (%)	$\rho_{xx}(0)$ ($\mu\Omega$ cm)	$\Delta\rho_{xx}$ ($\mu\Omega$ cm)	n_H (10^{22} cm^{-3})	λ_{eff} (Å)
Fe-Ag series								
Fe_4Ag_{96}	As	4.2	II	14.6	19.0	2.77	4.60	52.3
Fe_7Ag_{93}				19.8	31.9	6.32	4.30	32.6
$Fe_{13}Ag_{87}$				28.6	36.7	10.5	3.17	34.7
$Fe_{17}Ag_{83}$				30.3	38.0	11.5	3.13	33.8
$Fe_{24}Ag_{76}$				29.1	36.6	10.7	3.03	35.8
$Fe_{33}Ag_{67}$				12.5	37.4	4.68	3.08	34.7
$Fe_{43}Ag_{57}$				3.89	38.4	1.50	3.21	32.9
$Fe_{54}Ag_{46}$				1.57	39.2	0.63	3.63	29.7
$Fe_{71}Ag_{29}$				1.18	39.4	0.47	5.47	22.5
$Fe_{13}Ag_{87}$	As	4.2	II	28.6	36.7	10.5	3.17	34.7
	250			36.5	16.1	5.89	3.82	69.7
	325			15.4	8.83	1.36	4.83	109
	400			6.40	5.13	0.33	5.54	171
	475			0.00	4.03	0.01	5.23	226
$Fe_{20}Ag_{80}$	As	4.2	II	27.9	30.9	8.63	3.45	38.9
	As		I	21.5	27.4	5.89	4.64	36.1
	200			22.2	17.5	3.88	5.12	52.9
	250			18.6	13.4	2.49	5.73	64.1
	300			12.9	10.1	1.30	6.44	78.6
	350			8.53	8.08	0.69	6.45	98.1
	400			5.78	7.04	0.41	7.16	105
	450			1.31	5.95	0.08	7.46	121
	As	77		15.4	28.4	4.38	5.20	32.2
	200			15.8	18.1	2.87	5.29	49.9
	250			13.7	14.0	1.91	5.89	60.4
	300			10.2	10.5	1.07	6.64	73.8
	350			6.68	8.53	0.57	6.61	91.4
	400			1.19	6.72	0.08	6.98	112
	450			0.16	6.26	0.01	7.15	118
	As	300	I	6.59	31.3	2.06	9.06	20.2
	200			6.99	20.4	1.43	7.23	36.0
	250			5.89	16.0	0.94	7.52	44.9
	300			4.22	12.3	0.52	8.06	55.4
	350			2.63	10.3	0.27	7.30	71.1
	400			0.70	8.60	0.06	6.96	87.6
	450			0.09	8.16	0.01	7.41	88.6
Fe-Cu series								
$Fe_{10}Cu_{90}$	As	4.2	II	14.9	29.8	4.44	8.95	21.4
	250			13.9	12.7	1.77	10.8	44.3
	325			11.9	10.94	1.30	10.9	51.1
	400			3.4	7.31	0.25	12.4	70.3
$Fe_{20}Cu_{80}$	As			15.7	45.8	7.18	5.08	20.3
$Fe_{30}Cu_{70}$				10.0	58.6	5.87	4.92	16.2
$Fe_{50}Cu_{50}$				2.9	55.8	1.60	6.44	14.2
Fe-Au series								
Fe_7Au_{93}	As	4.2	II	10.9	50.2	5.45	5.66	17.2
$Fe_{15}Au_{85}$				22.5	56.8	12.7	7.22	12.9
$Fe_{23}Au_{77}$				12.2	38.7	4.67	5.57	22.6
$Fe_{41}Au_{59}$				1.21	29.6	0.38	5.42	30.0

TABLE II. (*Continued*).

Sample	T_A (°C)	T (K)	SM	MR (%)	$\rho_{xx}(0)$ ($\mu\Omega$ cm)	$\Delta\rho_{xx}$ ($\mu\Omega$ cm)	n_H (10^{22} cm^{-3})	λ_{eff} (Å)
Co-Ag series								
$Co_{20}Ag_{80}$	As[a]	4.2	I	37.1	20.9	7.73	4.27	50.1
	200			37.9	22.1	8.36	4.24	47.5
	330			45.6	13.8	6.30	4.03	78.4
	480			40.2	9.26	3.73	3.99	118
	605			33.3	7.22	2.41	4.01	151
	As[a]	77		32.0	20.9	6.68	4.23	50.2
	200			32.0	22.1	5.94	4.30	47.0
	330			39.5	14.2	4.99	4.27	73.0
	480			35.7	9.64	3.15	4.23	109
	605			29.0	9.76	3.15	4.69	151

[a]as-sputtered at liquid-nitrogen temperature.

terial dependent. The slow linear change with H in the high-field region ($H > 2$ T) is the normal Hall resistivity ρ_{xy}^0 and is inversely proportional to the carrier density n_H, i.e. the Hall coefficient $R_0 = \rho_{xy}^0/H = 1/n_H ec$. With the Drude-Sommerfeld formula $\rho_{xx} = m^* v_F/n_H e^2 \lambda_{\text{eff}}$ and $v_F = \hbar\sqrt[3]{3\pi^2 n_H}/m^*$, the effective mean free path λ_{eff} can be derived from experimental values of n_H. Here m^* is the effective mass of electrons, and v_F the Fermi velocity. In Table II, the values of n_H and λ_{eff} obtained from analysis of Hall-effect data are listed for all of the samples. We have also shown the values of λ_{eff} ($T = 4.2$ K) in Fig. 2 for $Fe_{20}Ag_{80}$ samples annealed at various temperatures. As shown in Table II and Fig. 2, λ_{eff} is rather short for as-sputtered samples (≈30–40 Å). However, as the annealing temperature is increased, λ_{eff} increases too, as expected. In general, λ_{eff} is larger than the magnetic particle size but less than the grain size of the nonmagnetic phase (e.g., Ag). The resistivity of the as-sputtered samples is quite high compared to that of pure metals. This is mainly caused by the short λ_{eff} in our systems.

The measured magnetization M versus magnetic field H (Fig. 6, lower panels) demonstrates the magnetic saturation process and hysteresis of the magnetic granular materials. About 90% saturation is achieved at fields 0.5–1 T. The variation of ρ_{xx} with H correlates with the variation of M. In particular, whenever there is a large (small) hysteresis in M, a large (small) hysteresis is also present in ρ_{xx}.

Based on Table II, we present in Fig. 7 the volume-fraction dependence of GMR for the Fe-Ag, Fe-Cu, Fe-Au, Fe-Pt, and Co-Ag series, all prepared without post-deposition thermal annealing. A portion of the data for the Co-Ag series was adopted from Ref. 30. Except for the Fe-Pt series, which forms concentrated alloys, the volume-fraction dependence of GMR for the alloy systems demonstrates some universal features: (1) In the magnetically dilute region, the MR increases with x due to the increasing concentration of magnetic scattering centers; (2) At x= 0.15–0.25, the MR reaches a maximum with the largest GMR effect in each series; (3) As x further increases beyond the peak region, the MR drops with increasing x, approaching a very small value. It is observed that the GMR ≈ 0 at $x \to 1$. We believe that this trend is due to the increasing coalescence of magnetic particles. As x increases, it is more likely for magnetic particles to connect to adjacent ones to form cluster networks. In fact, above the percolation threshold x_c a cluster network of infinite extension is formed. For a random three-dimensional system, x_c is on the order of 0.2. However, x_c is system dependent. For a two-phase granular solid lacking the so-called black and white symmetry (interchanging the two components results in a change in morphology), x_c may differ from 0.2. As the magnetic particles coalesce, the clusters form multido-

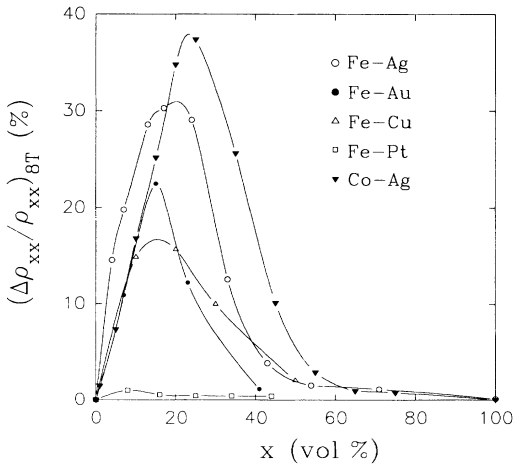

FIG. 7. Values of GMR ($\Delta\rho_{xx}/\rho_{xx}$) versus the magnetic volume fraction x for as-sputtered samples of Fe-Ag (open circles), Co-Ag (filled triangles), Fe-Au (filled circles), Fe-Cu (open triangles), and Fe-Pt (open squares). $T = 4.2$ K. The lines are guides to the eye.

main structures.[31] Consequently, GMR diminishes for the same reason that in a bulk multidomain magnetic metal MR is in general a minute value. In addition, the reduced effective surface area of a large cluster is also a cause of the reduced GMR effect, because magnetic-surface scattering plays a dominant role, as will be discussed later.

The effect of percolation can also manifest itself in other magnetic parameters of a granular solid. Among them, magnetic coercivity H_c is most sensitive to the particle percolation. For independent single-domain particles, H_c is rather large as a result of the combination of shape, crystalline, and strain anisotropies. As particles start to coalesce, H_c will be reduced due to the formation of multidomainlike structure.[31] Figure 8 shows the value of H_c of the as-sputtered Fe_xAg_{100-x} series as a function of x measured at $T = 5.0$ K. In the low-x region ($x < 0.2$), H_c remains relatively constant at about 350 G. At $x \approx 0.2$, H_c starts to decrease with increasing x, approaching the value of bulk polycrystalline Fe (a few tens of gauss). The decrease of H_c with x in the region $x \geq 0.2$ coincides exactly with the peak of $\Delta\rho_{xx}/\rho_{xx}$ in Fe_xAg_{100-x}. Since H_c has no direct relationship with $\Delta\rho_{xx}/\rho_{xx}$, the coincidence of the concurrent dependence of these two quantities on the volume fraction lends strong support to the view that particle percolation is the cause for the suppression of both $\Delta\rho_{xx}/\rho_{xx}$ and H_c at large x.

Among the many systems studied, only the Fe-Pt series failed to exhibit the GMR effect. This null result supports the conjecture that the granular nature of a magnetic alloy is a crucial requirement for GMR. Other series with GMR are all immiscible or nearly immiscible alloys, and, therefore, have substantial magnetic inhomogeneities. The Fe_xPt_{100-x} system has many intermetalic alloys in its phase diagram.[32] The sputtering technique yields metastable Fe-Pt solid solutions across the whole concentration range. All of our Fe-Pt samples are strongly ferromagnetic with low saturation fields. This indicates long-range magnetic ordering. The randomness of single-domain moments is therefore nonexistent in Fe-Pt, a requirement most crucial to the GMR effect.

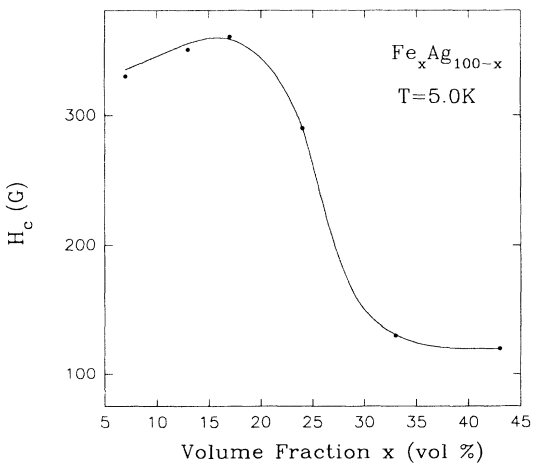

FIG. 8. Coercivity H_c versus Fe volume fraction x for the as-sputtered Fe-Ag series. $T = 5$ K.

We next turn our attention to the effects of thermal annealing on MR in granular systems. Annealing studies were carried out for $Fe_{13}Ag_{87}$, $Fe_{20}Ag_{80}$, $Fe_{10}Cu_{90}$, and $Co_{20}Ag_{80}$ samples. The detailed results are presented in Table II. Here, we limit our discussion to the $Fe_{20}Ag_{80}$ samples annealed at $T_A = 200$, 250, 300, 350, 400, 450, and 500 °C in high vacuum for 15 min. Results of other systems are qualitatively similar to those for the $Fe_{20}Ag_{80}$ series. The microstructure and magnetic properties of the annealed $Fe_{20}Ag_{80}$ samples have been presented in earlier sections. Data of grain size and magnetic particle size are shown in Fig. 2.

Figure 9 displays the MR in sweeping H for the as-sputtered and annealed $Fe_{20}Ag_{80}$ samples at three measuring temperatures, $T = 4.2$, 77, and 300 K. The evolution of $\Delta\rho_{xx}/\rho_{xx}$ with the annealing and measuring temperatures is clearly evident. Thermal annealing, which enlarges the magnetic particle size, diminishes the GMR effect gradually. However, annealing does yield a smaller saturation field for the MR. High measuring temperature also decreases the $\Delta\rho_{xx}/\rho_{xx}$ value, as expected. Thermal disturbances not only randomize magnetic alignment via superparamagnetism, but also enhance resistivity due to electron-phonon interaction.

We have extracted three important parameters, $\Delta\rho_{xx}/\rho_{xx}$, $\rho_{xx}(0)$, and $\Delta\rho_{xx} = \rho_{xx}(0\text{ T}) - \rho_{xx}(8\text{ T})$ from Fig. 9 and plotted them in Fig. 10 as functions of T_A. Both $\Delta\rho_{xx}$ and ρ_{xx} decrease monotonically with T_A. However the ratio $\Delta\rho_{xx}/\rho_{xx}$ increases slightly at low T_A and then decreases at high T_A. This is because the denominator ρ_{xx} decreases with T_A more rapidly at low T_A than $\Delta\rho_{xx}$ does. For this reason, $\Delta\rho_{xx}$ is a better parameter to characterize the GMR effect, because it is mainly caused by the magnetic scattering. Thermal annealing has three major consequences: It reduces structural disorder, enlarges particle size, and increases interparticle separation. As a result, the electron mean free path will increase, causing the absolute resistivity ρ_{xx} to decrease as shown in the lower panel of Fig. 10. The suppression of $\Delta\rho_{xx}$ at high T_A is mainly due to the reduction of the spin-dependent scattering as a result of the enlarged particle size. In Fig. 11(a), we plot $\Delta\rho_{xx}$ vs the inverse of the magnetic particle diameter $1/2r_0$ at $T = 4.2$, 77, and 300 K. It is evident that $\Delta\rho_{xx}$ is inversely proportional to the particle size, i.e. $\Delta\rho_{xx} \propto 1/r_0$. This can be understood only if we assume that magnetic scattering occurs primarily on the surface of the magnetic particles. In such a case $\Delta\rho_{xx}$ is linearly dependent on the surface-to-volume ratio of the particles, which is proportional to $1/r_0$. In other words, the larger the magnetic particle, the smaller the number of magnetic scatterers on the surface, and, therefore, the smaller the cross section of the magnetic scattering. The absolute resistivity $\rho_{xx}(0\text{ T})$ also seems to correlate with $1/r_0$, except for the as-sputtered sample, as shown in Fig. 11(b). This is because the electron mean free path λ_{eff} roughly follows the size of the magnetic particles as evidenced in Fig. 2, and $\rho_{xx}(0\text{ T})$ scales with $1/\lambda_{\text{eff}}$. In the as-sputtered sample, excess disorder causes ρ_{xx} vs $1/r_0$ to deviate from the linear relation.

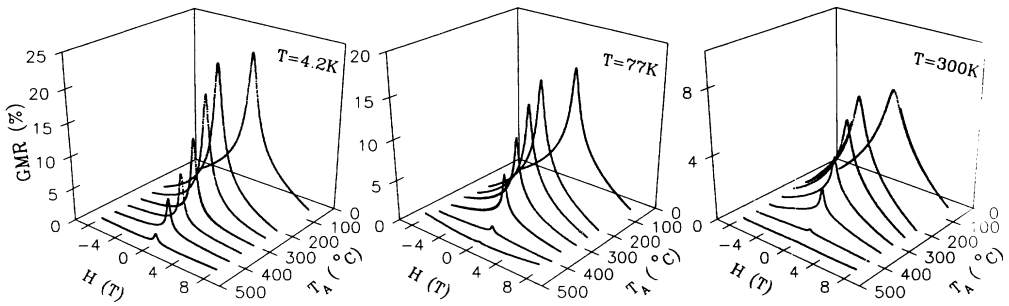

FIG. 9. GMR $[\rho_{xx}(H) - \rho_{xx}(8T)]/\rho_{xx}(0)$ versus H for $Fe_{20}Ag_{80}$ annealed at various temperatures T_A. Results are given for measurements at 4.2 K (left), 77 K (middle), and 300 K (right).

VI. ANALYSIS AND DISCUSSION

In this section we will attempt to understand the basic mechanism of the spin-dependent scattering responsible for GMR in granular materials. One can proceed with two different approaches. In the large-particle limit (e.g., $2r_0 > 100$ Å), the sensible approach is to consider magnetic and nonmagnetic scatterings both at the interface and in the bulk of the particles and the matrix. This is the method adopted by the semiclassical approach[13] and by the quantum Kubo calculation[14] to solve GMR problems in multilayers. The problems associated with these methods are that there are so many parameters, such as interface scattering coefficients and various scattering lengths, that a quantitative comparison with the experimental results is difficult.

In the extreme case of dilute magnetic alloys, MR in many systems[33–35] has been successfully explained by considering the effective exchange interaction between conduction electrons and scattering magnetic centers.[36–38] One expects that this method could be extended to granular systems with small magnetic particles, particularly for the as-sputtered or mildly annealed samples where the particles are a few tens of angstroms in size. This is the starting point of our analysis.[39] We do not expect this analysis to be valid for samples annealed at high temperatures, in which the magnetic particles are quite large. But the model should provide us with a qualitative trend for the evolution process of the magnetotransport properties with annealing.

The scattering potential experienced by the conduction electrons in dilute magnetic alloys is of the following form:

$$H = V(\mathbf{r}) - 2J(\mathbf{r})\mathbf{s}\cdot\mathbf{S}, \tag{6}$$

where $V(\mathbf{r})$ describes the spin-independent interaction and $J(\mathbf{r})$ the exchange interaction between the electrons with spin $\mathbf{s}$ and the magnetic scatterers with spin $\mathbf{S}$. This interaction Hamiltonian has also been used to describe the GMR effect in magnetic multilayers. We assume that it is also applicable to magnetic granular solids after some modifications. Because of the finite size of the magnetic particles, the effective spin $\mathbf{S}'$ affecting the conduction electrons is only a portion of the total spin $\mathbf{S}$ of a magnetic particle. If surface scattering is dominant, then $\mathbf{S}'$ will be mostly confined on the surface. However, $\mathbf{S}'$ and $\mathbf{S}$ are not independent. The single-domain nature of the particles requires that $\mathbf{S}'$ and $\mathbf{S}$ share the same orientation and dynamics. In this sense, the conduction electron interacts indirectly with the magnetic particle as a whole. We introduce a modified exchange interaction as

$$H = V - 2JS'\mathbf{s}\cdot\boldsymbol{\sigma}(\mathbf{S}), \tag{7}$$

where $\boldsymbol{\sigma}(\mathbf{S}) = \mathbf{S}/S$ is the unit vector of $\mathbf{S}$. Because of the large magnitude of the giant spin $\mathbf{S}$, $\boldsymbol{\sigma}(\mathbf{S})$ is a classical

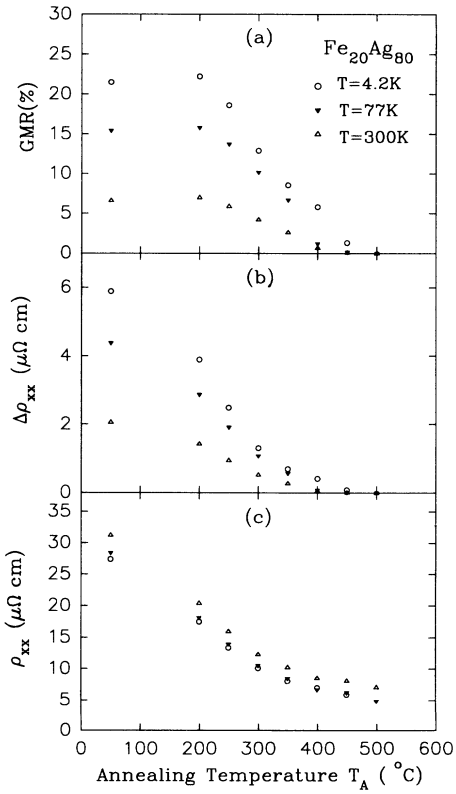

FIG. 10. (a) Measured GMR, (b) net change in resistivity $\Delta\rho_{xx}$, and (c) zero-field resistivity $\rho_{xx}(0)$ for $Fe_{20}Ag_{80}$ as a function of annealing temperature T_A. Measurement temperature is 4.2 K (circles), 77 K (filled triangles), and 300 K (open triangles).

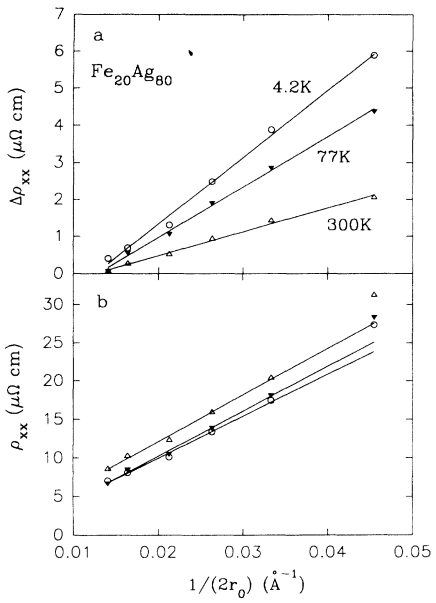

FIG. 11. (a) Net change in resistivity $\Delta\rho_{xx}$ and (b) zero-field resistivity $\rho_{xx}(0)$ versus the inverse of Fe particle diameter $1/(2r_0)$, for different annealed $Fe_{20}Ag_{80}$ samples measured at 4.2 K (circles), 77 K (filled triangles), and 300 K (open triangles).

vector whose orientation is determined by the magnetic field, magnetic anisotropy, and temperature.

To evaluate the spin-dependent scattering in granular systems, we proceed in the same way as in the problem of electron transport in dilute magnetic alloys.[37] We use the first-order Born approximation and neglect the effects of multiple scattering. The electron distributions in the steady state are in detailed balance in the scattering process. When the scattering potential (7) is applied to the scattering matrices, considering both the spin-preserving and spin-flipping processes, the spin-dependent electron scattering rate is found to be

$$1/\tau_{\pm} = A\{1 \pm B(M/M_s) - (C/S)\tanh(\alpha/2)(M/M_s) \mp C\tanh(\alpha/2)[1 - \langle M^2\rangle/M_s^2] \pm (C/S)(M/M_s)\} . \quad (8)$$

Here, the plus and minus signs stand for spin up and spin down, respectively. The scattering matrix about the Fermi surface is approximated as isotropic. In Eq. (8), $M_s = gSN_m\mu_B$ and $M = M_s\langle\cos\theta\rangle$. Here g is the spectroscopic splitting factor, N_m the density of the magnetic particles, θ the angle between the magnetic field vector and the moment vector of a magnetic particle, and $\langle\cdots\rangle$ an average over all particles. The coefficients in the equation depend on the parameters in the scattering potential (7) as follows

$$A = \frac{mk_FN_m}{\pi\hbar^3}[V^2 + J^2S'^2], \quad (9)$$

$$B = 2(JS'/V)/[1 + (J/V)^2S'^2], \quad (10)$$

$$C = (JS'/V)^2/[1 + (J/V)^2S'^2], \quad (11)$$

$$\alpha = \frac{g\mu_BH}{k_BT}. \quad (12)$$

An external magnetic field, in general, has small effects on the coefficients A, B, and C, but it controls the spin-dependent scattering rate via $M(H)$, $\langle M^2(H)\rangle$, and α. Given a magnetic state such as a superparamagnetic or a frozen state, $M(H)$ and $\langle M^2(H)\rangle$ become well defined and so does $1/\tau_{\pm}$. The first two terms in relation (8) are due to spin-preserving scattering. The spin-flipping scattering is incorporated in the rest of the terms, which we have estimated to be less than 10% of the second term in our samples. In the following, we will neglect the spin-flipping interaction. This will simplify the expression for resistivity, and it is also an approximation adopted in the theoretical studies of GMR in magnetic multilayers.[40] Based on relation (8), and assuming that conduction electrons in the spin-up and spin-down states are equally populated, the resistivity in granular solids is of the form

$$\rho_{xx} = \rho_0[1 - B^2M^2/M_s^2] + \rho_d, \quad (13)$$

where $\rho_0 = m^*A/ne^2$ and ρ_d is the partial resistivity caused by nonmagnetic mechanisms, e.g. disorders and phonons. The GMR is then of the form

$$\frac{\Delta\rho_{xx}}{\rho_{xx}} = \frac{\rho_{xx}(0\text{ T}) - \rho_{xx}(H)}{\rho_{xx}(0\text{ T})} = \frac{B^2M^2}{M_s^2(1 + \rho_d/\rho_0)}. \quad (14)$$

The MR defined here is minus of the usual definition. We note that the resistivity due to magnetic scattering depends on the magnetic state through the magnetization M only. The dependence of $\Delta\rho_{xx}/\rho_{xx}$ on M is quadratic, i.e. $\Delta\rho_{xx}/\rho_{xx} \propto M^2$ as was shown[8] by Xiao *et al.* for Co-Cu granular systems. The coefficient B^2 depends only on the product of J/V and the effective spin S', i.e. $\gamma = JS'/V$. The role of the total spin S of the magnetic particles is in the magnetization M and therefore it affects the saturation process of the GMR. The larger the magnetic particles are, the easier the saturation process is for both M and $\Delta\rho_{xx}/\rho_{xx}$, in agreement with the experimental observation. As shown in Fig. 9, at a particular temperature the saturation of $\Delta\rho_{xx}/\rho_{xx}$ becomes easier to achieve as the size of the magnetic particles is made larger by thermal annealing.

With the introduction of the new parameter $\gamma = JS'/V$, relation (14) can be expressed as

$$\Delta\rho_{xx}/\rho_{xx} = \frac{4\gamma^2}{(1 + \gamma^2)^2}\frac{1}{(1 + \rho_d/\rho_0)}\frac{M^2}{M_s^2}. \quad (15)$$

The field dependence of $\Delta\rho_{xx}/\rho_{xx}$ is caused by $[M(H)/M_s]^2$ which has been measured as the magnetic hysteresis curves for our samples. Using relation (15) and the measured $M(H)$, we have fitted our measured $\Delta\rho_{xx}/\rho_{xx}$ versus magnetic field at $T = 4.2$, 77, and 300 K for $Fe_{20}Ag_{80}$ and $Co_{20}Ag_{80}$ samples with different T_A's. The fitting parameters are γ and ρ_d/ρ_0. The results of the fittings for three representative $Fe_{20}Ag_{80}$ samples are shown in Fig. 12, where the dots are the measured data

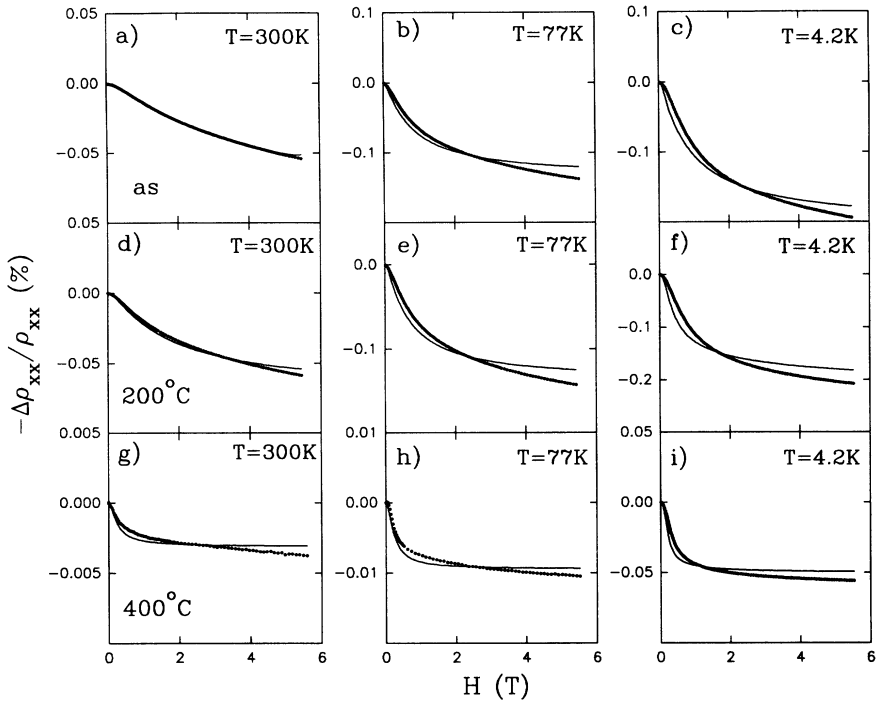

FIG. 12. Magnetoresistance data versus magnetic field H for $Fe_{20}Ag_{80}$ with different annealing conditions: (a), (b), (c) as sputtered, (d), (e), (f) $T_A = 200\,^\circ$C, and (g), (h), (i) $T_A = 400\,^\circ$C. The measurement temperatures are 4.2, 77, and 300 K as indicated. The solid curves are fitting results using the modified effective exchange-interaction model.

and the solid lines are the fitted curves. As defined by (14) and (15) $\Delta\rho_{xx}/\rho_{xx}$ is always positive in our systems since $\rho_{xx}(H)$ decreases with H. To demonstrate the trend of $\rho_{xx}(H)$, however, we show $-\Delta\rho_{xx}/\rho_{xx}$ in Fig. 12 instead.

It is observed that relation (15) describes the experimental results reasonably well. Both the magnitude and the gradual saturation of $\Delta\rho_{xx}/\rho_{xx}$ are well accounted for in a wide range of temperatures ($T = 4.2 - 300$ K). The discrepancy between experimental data and theory is expected because of the following reasons: (1) The theory is an extended version of the model for magnetic diluted alloys, and is, therefore, limited to smaller particles; (2) Some weaker scattering mechanisms are neglected, such as spin flipping, weak-localization effect, field-induced orbital variations, and higher-order scattering; (3) The theory assumes uniform particle size, whereas, in reality, size distribution is unavoidable.

A further testing of relation (15) is presented in Fig. 13 for a $Co_{20}Ag_{80}$ sample which has a large magnetic hysteresis ($H_c \sim 3$ kG). The fitted $\Delta\rho_{xx}/\rho_{xx}$ follows the experimental data very well with the hysteresis in $\Delta\rho_{xx}/\rho_{xx}$ well accounted for.

The derived parameters $\gamma = JS'/V$ and ρ_d/ρ_0 from our fittings are listed in Table III for a series of $Fe_{20}Ag_{80}$ samples and some $Co_{20}Ag_{80}$ samples. We observe that, for any given sample, the value of ρ_d/ρ_0 increases with T. This is expected because at high T the phonon contribution to ρ_d is appreciable. The value of γ is also T dependent as a result of $S'(T)$ (J/V is approximately T independent). Since S' is part of the total spin S of a magnetic particle, the T dependence of S' should follow that of $M_s(T)$, i.e. $\gamma(T) \propto S'(T) \propto M_s(T)$. This leads to the equality $\gamma(T_1)/\gamma(T_2) = M_s(T_1)/M_s(T_2)$. The γ ratios $\gamma(4.2\text{ K})/\gamma(77\text{ K})$ and $\gamma(4.2\text{ K})/\gamma(300\text{ K})$ from theoretical fittings and the M_s ratios $M_s(4.2\text{ K})/M_s(77\text{ K})$ and $M_s(4.2\text{ K})/M_s(300\text{ K})$ obtained from measurements are also listed in Table III. Given the accuracies ($\pm 10\%$) of the measurements and the model, the above equality is well satisfied for all samples except for one $Fe_{20}Ag_{80}$ sample annealed at 400 °C. In this sample, the value of $\Delta\rho_{xx}/\rho_{xx}$ is very small. Other scattering mechanisms

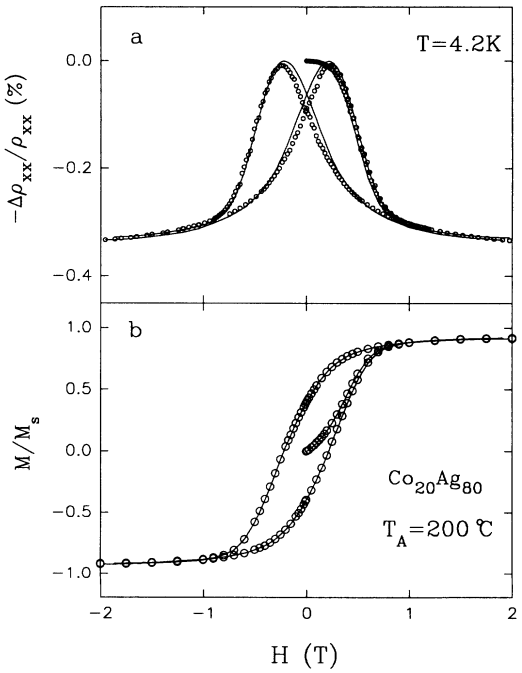

FIG. 13. (a) Measured (dots) and fitted (solid curves) MR for $Co_{20}Ag_{80}$ (annealed at 200 °C) at $T = 4.2$ K. (b) Magnetic hysteresis curves M obtained with H perpendicular to the sample plane at $T = 5$ K.

TABLE III. Fitted parameters γ, ρ_d/ρ_o for $Fe_{20}Ag_{80}$ and $Co_{20}Ag_{80}$ samples at different temperatures. The ratio $\gamma_{T_1}/\gamma_{T_2}$ is compared with the ratio $M_s(T_1)/M_s(T_2)$ for Fe-Ag.

Samples	γ			ρ_d/ρ_o			$\frac{\gamma_{4.2}}{\gamma_{77}}$	$\frac{M_s(4.2\text{ K})}{M_s(77\text{ K})}$	$\frac{\gamma_{4.2}}{\gamma_{300}}$	$\frac{M_s(4.2\text{ K})}{M_s(300\text{ K})}$
T_A(°C)	4.2 K	77 K	300 K	4.2 K	77 K	300 K				
					$Fe_{20}Ag_{80}$					
As	0.250	0.206	0.173	0.07	0.14	0.52	1.21	1.32	1.45	1.46
200	0.255	0.207	0.166	0.08	0.13	0.62	1.23	1.02	1.54	1.21
250	0.221	0.289	0.152	0.04	0.33	0.84	1.17	1.28	1.45	1.35
300	0.196	0.177	0.133	0.25	0.48	1.24	1.11	1.15	1.47	1.40
350	0.174	0.161	0.115	0.51	0.69	1.73	1.08	1.07	1.51	1.31
400	0.154	0.094	0.068	0.80	2.63	4.72	1.64	1.08	2.28	1.20
					$Co_{20}Ag_{80}$					
As	0.445	0.404		0.52	0.64					
200	0.464	0.422		0.42	0.59					

probably dominate over the magnetic scattering process and render the model inapplicable to this particular sample.

The T dependence of M_s is due to spin-wave excitations. Therefore, in order to minimize the reduction of GMR at elevated T, ferromagnetic materials with stiff spin-wave constants and high magnetic ordering temperatures (T_c) are much preferred. A stable M_s will make the $\frac{4\gamma^2}{(1+\gamma^2)^2}$ factor in relation (15) weakly T dependent. Another route to enhance $\Delta\rho_{xx}/\rho_{xx}$ is to minimize ρ_d as much as possible by using high-quality pure metals with weak electron-phonon interaction strengths.

At this point, a discussion about the role of superparamagnetism in GMR is called for. According to relation (15), superparamagnetism manifests itself only in the saturation process of $\Delta\rho_{xx}/\rho_{xx}$ or M. It does not fundamentally affect the saturated value of $\Delta\rho_{xx}/\rho_{xx}$ as $\frac{M}{M_S} \to 1$. In order to achieve a small saturation field in the superparamagnetic state, a magnetic material with a large atomic moment is needed to enhance the magnetic energy versus the thermal energy. In the frozen magnetic state, magnetic anisotropy (surface, crystalline, and shape, etc.) affects the saturation field more directly. The superparamagnetic transition is not expected to affect GMR. This is because the electron relaxation rate is much faster than that of the dynamic single-domain moments. As far as the conduction electrons are concerned, the single-domain moments remain frozen even in the superparamagnetic state defined in the conventional time scale (~1 sec) of a magnetometer.

Overall, relation (15) provides a good description of GMR in magnetic granular materials regardless of the actual magnetic state in the magnetic particles. Another good feature of relation (15) is that it allows us to estimate the maximum achievable GMR for a chosen material and the optimal range of γ. Under the condition that $\rho_d/\rho_0 \ll 1$, the saturated GMR ($M/M_s \to 1$) is

$$(\Delta\rho_{xx}/\rho_{xx})_s = \frac{4\gamma^2}{(1+\gamma^2)^2}. \tag{16}$$

Figure 14 plots the dependence of $(\Delta\rho_{xx}/\rho_{xx})_s$ on γ. $(\Delta\rho_{xx}/\rho_{xx})_s$ increases with γ up to a maximum value of 100% at $\gamma = 1$. It then decreases with γ as $\gamma > 1$. To compare with the experiment, we have included experimental values of $(\Delta\rho_{xx}/\rho_{xx})_s$ in Fig. 14 for both $Fe_{20}Ag_{80}$ and $Co_{20}Ag_{80}$ samples. The saturated values of $(\Delta\rho_{xx}/\rho_{xx})_s$ were derived by extrapolating the measured GMR within finite field range (≤ 8 T) to saturation by using a combination of normal and Lorentzian functions. The nonmagnetic contributions determined from the fittings were subtracted so that a direct comparison with relation (16) can be made. It is observed in Fig. 14 that the experimental values follow the postulated relationship rather well. The reason that the $Co_{20}Ag_{80}$ samples have substantially higher GMR than $Fe_{20}Ag_{80}$ is that the γ value in $Co_{20}Ag_{80}$ is much larger. However, there is still room to increase GMR much further by searching for binary systems with $\gamma \sim 1$.

There are a few possible routes to increase $\gamma = JS'/V$. A larger exchange J and effective spin S' would benefit GMR enhancement. Reducing V is another possibility.

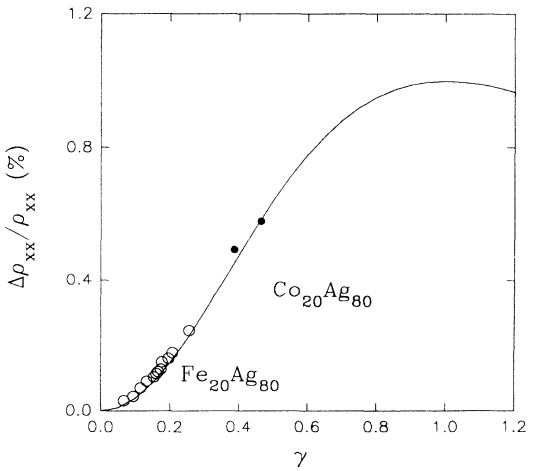

FIG. 14. Dependence of $\Delta\rho_{xx}/\rho_{xx}$ on the parameter $\gamma = JS'/V$ (solid curve) predicted by the modified effective exchange-interaction model. The open circles and the filled circles represents data of $Fe_{20}Ag_{80}$, and $Co_{20}Ag_{80}$, respectively, with various T_A's.

In $Fe_{20}Ag_{80}$ and $Co_{20}Ag_{80}$, γ is on the order of 0.2 to 0.4. We could not determine the values of J/V and S' separately in our analysis. In the literature,[34–36] J/V = 0.1–0.5 for transition-metal impurities in noble metals. If we assume that this range of J/V is about the same in our samples, the estimated S' is on the order of S' = 0.3–3.0. Thus the effective scattering seen by the scattered electron is atomic in size, not the whole magnetic particle. Presumably, the surfaces of the magnetic particles are the most effective scatterers.

VII. SUMMARIES AND CONCLUSIONS

We have systematically investigated the microstructure, magnetic properties, and giant magnetoresistance of a series of transition-metal granular solids. These materials, made by magnetron sputtering, consist of nanometer-sized magnetic transition-metal particles (Fe or Co) embedded in a nonmagnetic metallic matrix (Cu, Ag, or Au). A wide range of samples with various particle volume fractions and thermal annealing conditions have been prepared and studied with the objective of understanding the origin of the spin-dependent scattering which causes GMR. We have also presented a host of important transport parameters for every sample studied.

Among the five systems studied, the four immiscible systems (Fe-Ag, Fe-Cu, Fe-Au, and Co-Ag) exhibit GMR. A universal variation of GMR with particle volume fraction has been uncovered. There is always a peak of GMR at a volume fraction of 15–25%, near the percolation threshold. The decrease of GMR at high concentrations is attributed to the increasing coalescence of the magnetic particles. One system which does not show GMR is Fe-Pt and is a solid-solution alloy, indicating that phase separation is crucial for GMR in magnetically heterogeneous materials.

Thermal annealing of as-sputtered samples is an effective way to enlarge the magnetic particle size. Without exceptions, $\Delta\rho_{xx}$ and ρ_{xx} always decrease with increasing annealing temperature. For systems to show appreciable GMR, small particles are preferred over large ones. Nevertheless, thermal annealing does have the advantage of reducing the saturation field for GMR. The field dependence and the temperature effect on GMR have been well accounted for by a modified effective exchange-interaction (MEEI) model, which was extended from a model of magnetic dilute alloys. The MEEI model predicts that MR is determined by three parameters, $\gamma = JS'/V$, ρ_d/ρ_0, and $M^2(H)$. To achieve maximum GMR, ρ_d due to nonmagnetic scattering should be reduced to its minimum, whereas γ should be as close to unity as possible. The Co-Ag samples, with the largest GMR among all the series studied, have a γ value of about 0.5, leaving parameter space for further enhancing the GMR. The saturated GMR value, according to the MEEI model, does not depend on the magnetic state of the particles (superparamagnetic or frozen state). However, the saturation process of MR is directly related to $[M(H,T)/M_s(T)]^2$. High temperature and large magnetic anisotropy are detrimental factors to the saturation process because they make the saturation of $M(H,T)$ difficult. Another prediction of the MEEI model is that the effect of temperature on the saturated GMR value is due to the temperature dependence of $\gamma(T) = JS'(T)/V$ and $\rho_d(T)/\rho_0$. A high temperature reduces $\gamma(T)$ because of spin-wave excitations (i.e. reducing $S'(T)$) and increased $\rho_d(T)$ (due to electron-phonon interaction); both are undesirable for the GMR effect.

ACKNOWLEDGMENTS

We would like to thank Peng Xiong and Kent Ibsen for helpful technical assistance. We are indebted to C. L. Chien for providing some $Co_{20}Ag_{80}$ samples. This work was supported by National Science Foundation Grants Nos. DMR-9121747 and DMR-9258306. G.X. wishes to thank the A.P. Sloan Foundation for support.

[1] M. N. Baibich, J. M. Broto, A. Fert, F. Nguyen Van Dau, F. Petroff, P. Etienne, G. Creuzet, A. Friederich, and J. Chazelas, Phys. Rev. Lett. **61**, 2472 (1988).
[2] G. Binasch, P. Grünberg, F. Saurenbach, and W. Zinn, Phys. Rev. B **39**, 4828 (1989).
[3] J. J. Krebs, P. Lubitz, A. Chaiken, and G. A. Prinz, Phys. Rev. Lett. **63**, 1645 (1989).
[4] S. S. P. Parkin, N. More, and K. P. Roche, Phys. Rev. Lett. **64**, 2304 (1990); S. S. P. Parkin, R. Bhadra, and K. P. Roche, Phys. Rev. Lett. **66**, 2152 (1991).
[5] E. E. Fullerton, D. M. Kelly, J. Guimpel, and I. K. Schuller, Phys. Rev. Lett. **68**, 859 (1992).
[6] W. P. Pratt, Jr., S.-F. Lee, J. M. Slaughter, R. Loloee, P. A. Schroeder, and J. Bass, Phys. Rev. Lett. **66**, 3060 (1991); S. F. Lee, W. P. Pratt, Jr., R. Loloee, P. A. Schroeder, and J. Bass, Phys. Rev. B **46**, 548 (1992).
[7] A. E. Berkowitz, J. R. Mitchell, M. J. Carey, A. P. Young, S. Zhang, F. E. Spada, F. T. Parker, A. Hutten, and G. Thomas, Phys. Rev. Lett. **68**, 3745 (1992).
[8] J. Q. Xiao, J. S. Jiang, and C. L. Chien, Phys. Rev. Lett. **68**, 3749 (1992); Phys. Rev. B **46**, 9266 (1992).
[9] P. Xiong, Gang Xiao, J. Q. Wang, J. Q. Xiao, J. S. Jiang, and C. L. Chien, Phys. Rev. Lett. **69**, 3220 (1992).
[10] G. Bergmann, Z. Phys. B **48**, 5 (1982).
[11] D. Abraham and R. Rosenbaum, Phys. Rev. **B 27**, 1413 (1983).
[12] J. B. Bieri, A. Fert, G. Creuzet, and A. Schuhl, J. Phys. F **16**, 2099 (1986).
[13] R. E. Camley and J. Barnaś, Phys. Rev. Lett. **63**, 664 (1989); J. Barnaś, A. Fuss, R. E. Camley, P. Grünberg, and W. Zinn, Phys. B **42**, 8110 (1990).
[14] P. M. Levy, S. Zhang, and A. Fert, Phys. Rev. Lett. **65**, 1643 (1990); S. Zhang, P. M. Levy, and A. Fert, Phys. Rev. B **45**, 8689 (1992).
[15] S. Zhang and P. M. Levy, J. Appl. Phys. **69**, 4786 (1991).
[16] S. Zhang, Appl. Phys. Lett. **61**, 1855 (1992).
[17] H. E. Camblong and P. M. Levy, Phys. Rev. Lett. **69**, 2835 (1992).

[18] *Binary Alloy Phase Diagram*, edited by T. B. Massalski *et al.* (ASM International, Ohio, 1990), Vol. 1, pp. 25, 35, 367; Vol. 2, p. 1408.
[19] Gang Xiao and C. L. Chien, J. Appl. Phys. **61**, 3308 (1987).
[20] K. Sumiyama, T. Yoshitake, and Y. Nakamura, J. Phys. Soc. Jap. **53**, 3160 (1984); K. Sumiyama and Y. Nakamura, Phys. Status Solidi **81**, K109 (1984).
[21] C. L. Chien, S. H. Liou, D. Kofalt, W. Yu, T. Egami, and T. R. McGuire, Phys. Rev. B **33**, 3247 (1986).
[22] J. R. Childress, C. L. Chien, and M. Nathan, Appl. Phys. Lett. **56**, 95 (1990).
[23] C. Larica, E. M. Baggio-Saitovitch, S. K. Xia, J. Magn. Magn. Mater. **110**, 106 (1992).
[24] *Powder Diffraction File, Inorganic Phases*, edited by W. F. McClune *et al.* (JCPDS, Pennsylvania, 1982), p. 701, 4-0783.
[25] J. R. Childress and C. L. Chien, Appl. Phys. Lett. **56**, 1 (1990).
[26] E. P. Wohlfarth, in *Ferromagnetic Materials*, edited by E. P. Wohlfarth (North-Holland, New York, 1980), Vol. 1, p. 20.
[27] Derived from the empirical relation $\Delta M_s/M_s(0) = AT^{3/2}$ and the value of A for Fe given by C. Kittel, *Introduction to Solid State Physics* (Wiley, New York, 1986), p. 428.
[28] R. W. Chantrel and E. P. Wohlfarth, J. Magn. Magn. Mater. **40**, 1 (1983).
[29] L. Berger and G. Gergmann, in *The Hall Effect and its Applications*, edited by C. L. Chien and C. R. Westgate (Plenum, New York, 1980), p. 55.
[30] J. Q. Xiao, J. S. Jiang, and C. L. Chien, IEEE Trans. Magn. Trans. (to be published).
[31] Gang Xiao and C. L. Chien, Appl. Phys. Lett. **51**, 1280 (1987).
[32] *Iron-Binary Phase Diagram*, edited by O. Kubaschewski (Springer-Verlag, New York, 1982), p. 92.
[33] A. N. Gerritsen and J. O. Linde, Physica **17**, 573 (1951).
[34] H. Rohrer, Phys. Rev. **174**, 583 (1968).
[35] R. Berman and J. Kopp, J. Phys. F **3**, 847 (1973).
[36] K. Yosida, Phys. Rev. **107**, 396 (1957).
[37] T. van Peski-Tinbergen and A. J. Dekker, Physica **29**, 917 (1963).
[38] R. J. Harrison and M. W. Klein, Phys. Rev. **154**, 154 (1967).
[39] J.-Q. Wang, P. Xiong, and Gang Xiao, Phys. Rev. B **47**, 8341 (1993).
[40] S. Zhang and P. M. Levy, Phys. Rev. B **43**, 11048 (1991).

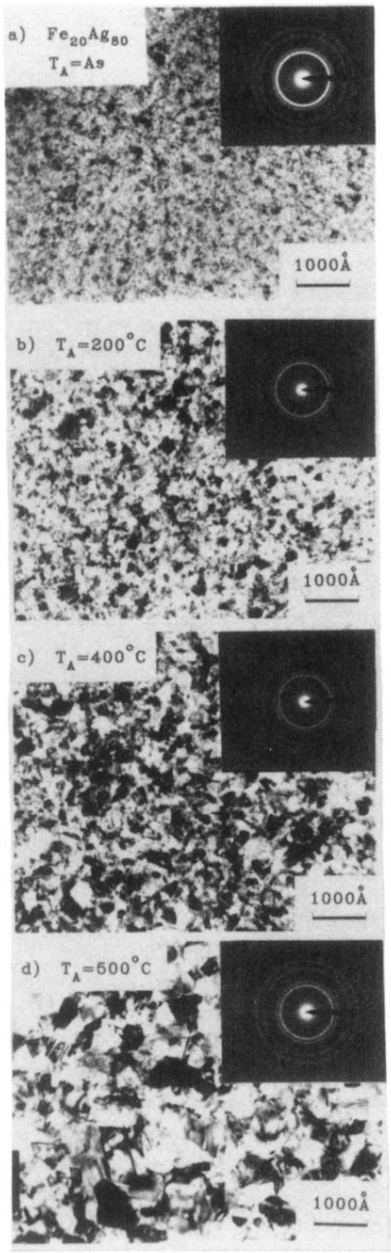

FIG. 1. Bright-field (TEM) images and selected-area diffraction patterns for $Fe_{20}Ag_{80}$ samples annealed at various temperatures T_A. (a) as-sputtered sample, (b) 200 °C, (c) 400 °C, and (d) 500 °C.

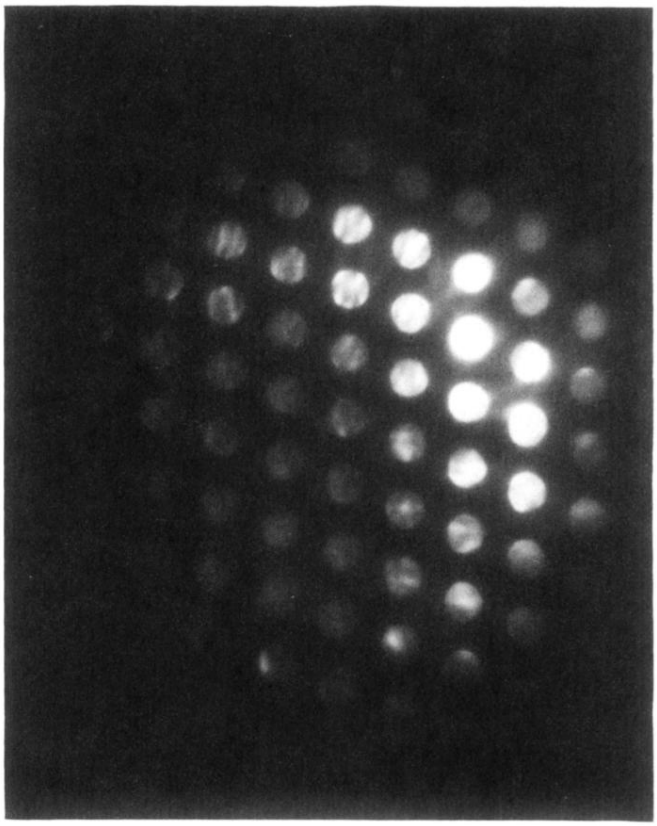

FIG. 3. Microdiffraction pattern of a Ag grain with zone axis [111] parallel to the electron beam.